

Tunable metamaterial beam using negative capacitor for local resonators coupling

Journal of Intelligent Material Systems and Structures

1–19

© The Author(s) 2019

Article reuse guidelines:

sagepub.com/journals-permissions

DOI: [10.1177/1045389X19891575](https://doi.org/10.1177/1045389X19891575)

[journals.sagepub.com/home/jim](http://jims.sagepub.com/home/jim)



Guobiao Hu¹, Jiawen Xu², Lihua Tang¹ , Chunbo Lan³ and Raj Das⁴

Abstract

This article presents a theoretical study of a tunable metamaterial beam for low-frequency broadband vibration suppression. First, the mechanism of employing the shunt circuit technique to realize the internal coupling between two adjacent local resonators is introduced. The working principle of the proposed metamaterial beam by integrating the shunt circuit technique is demonstrated. The stability of the proposed metamaterial beam is then analysed, and the corresponding criterion is proposed. Subsequently, analytical models of the proposed metamaterial beam are developed. The band structures and the transmittances are calculated. The analytical study demonstrates the generation of multiple band gaps using a shunt negative capacitance circuit, which is equivalent to a coupling spring. A parametric study is conducted to investigate the effect of the equivalent coupling stiffness on the band gaps and the corresponding suppression regions. It is found that the band gaps are controllable by varying the equivalent coupling stiffness. Finally, to verify the analytical solutions, a finite-element model of the proposed metamaterial beam is developed. The simulation results confirm the existence of multiple band gaps, which are tunable through modification of the negative capacitance. The broadband vibration-suppression ability of the proposed metamaterial beam is thus confirmed.

Keywords

Metamaterial, piezoelectric, vibration suppression, negative capacitor

I. Introduction

Similar to Bragg scattering of phononic crystals, elastic metamaterials with artificial micro-structures (i.e. embedded local resonators) can generate band gaps within which waves are restricted from propagation. One notable advantage of the local resonance-based elastic metamaterials is that their band gaps are directly related to the frequency of the local resonator, that is, irrelevant to the periodic constant. Consequently, the design of low-frequency band gaps in elastic metamaterials becomes physically easy to achieve by tuning the local resonators. Due to this fact, the application of elastic metamaterials for low-frequency vibration suppression has attracted numerous research interests in recent years (Banerjee et al., 2017; Chen et al., 2016; Cheng et al., 2013; Cheng and Shi, 2014; Hu et al., 2017b; Li et al., 2018; Liu et al., 2007; Zhu et al., 2014).

Although elastic metamaterials have the advantage of achieving low-frequency band gaps, the widths of band gaps of elastic metamaterials are usually relatively narrow. This significantly limits the application of elastic metamaterials in the circumstances where vibrations exist over a broadband spectrum. To address this issue,

various methods have been proposed by researchers to broaden the width of band gaps of elastic metamaterials. Starting from the local resonance mechanism for band gap generation, efforts have been devoted to introducing multiple local resonances for generating multiple band gaps in elastic metamaterials, such as integration of multiple degree-of-freedom local resonators (Huang and Sun, 2010; Xiao et al., 2012), utilization of multiple resonators with different natural frequencies (Zhu et al., 2014), and implementation of internal couplings between local resonators through

¹Department of Mechanical Engineering, The University of Auckland, Auckland, New Zealand

²Jiangsu Key Lab of Remote Measurement and Control, School of Instrument Science and Engineering, Southeast University, Nanjing, China

³College of Aerospace Engineering, Nanjing University of Aeronautics and Astronautics, Nanjing, China

⁴School of Engineering, RMIT University, Melbourne, VIC, Australia

Corresponding author:

Lihua Tang, Department of Mechanical Engineering, The University of Auckland, 20 Symonds Street, Auckland 1010, New Zealand.

Email: l.tang@auckland.ac.nz

spring connections (Hu et al., 2017b, 2018b). Recently, applying nonlinearity has been proposed to improve the band gap characteristics of linear metamaterial systems (Fang et al., 2016, 2017; Khajehtourian and Hussein, 2014; Lazarov and Jensen, 2007). As reported and explained by Fang et al. (2017), the introduction of nonlinearity can enable metamaterials to obtain new band gaps based on the mechanism of chaos.

Design of metamaterials with actively tunable band gaps is also an effective strategy for realizing the broadband vibration-suppression purpose. Chen et al. (2013) presented a metamaterial plate with piezoelectric patches shunted to resistive-inductive circuits. The plate has not only Bragg scattering-based band gaps but also a local resonance-based band gap. The results indicated that by manipulating the shunt resistive-inductive circuits, both Bragg scattering and local resonant band gaps were controllable. Based on a similar idea, Hu et al. (2017a) conducted a theoretical study of metamaterials with piezoelectric elements. According to their research, the metamaterial can realize broadband vibration suppression in strong coupling conditions by tuning the shunt resistance. Chen et al. (2014) proposed a band gap control method using piezoelectric elements as active springs. They shunted the piezoelectric elements to negative capacitance (NC) circuits. The effective stiffness of the piezoelectric element is controllable via the value of NC shunts; thus, the characteristics of the band gap can be changed accordingly. Zhu et al. (2016) then experimentally realized the idea presented in Chen et al. (2014). Li et al. (2018) designed a self-adaptive metamaterial beam with piezoelectric resonators. A feedback digital circuit is used to control the effective stiffness of the piezoelectric resonators, thus adaptively tuning the band gaps according to the input excitation. Additional related research can be found in studies of Chen et al. (2011, 2017), Thorp et al. (2001), Wang and Chen (2015), Xu and Tang (2017), Zhang et al. (2015), and Zhou et al. (2015). Besides the piezoelectric shunt technique, it is worth mentioning that the tunability or reconfigurability in electromagnetic metamaterials (Hand and Cummer, 2007; Liu and Padilla, 2013) utilizing microelectromechanical systems (MEMS) could also inspire the development of band gap tuneable acoustic-elastic metamaterials, which could be another promising way to realize the broadband vibration suppression.

Due to the simple implementation and electrical-mechanical transformation characteristics, the piezoelectric shunt technique has attracted numerous research interests for developing active tunable metamaterials in recent years. However, previous studies (Chen et al., 2011, 2013, 2014; Hu et al., 2017a; Thorp et al., 2001; Wang and Chen, 2015; Xu and Tang, 2017; Zhang et al., 2015; Zhou et al., 2015; Zhu et al., 2016) employed independent piezoelectric shunt circuits for each local resonator. In this article, we present the

design of a piezoelectric metamaterial beam in which the two adjacent local resonators are coupled through a shunt capacitance circuit, which is equivalent to a coupling spring. The advantages of this design is that the employment of the piezoelectric shunt technique not only realizes the tunability but also provides a mechanism for generating multiple band gaps. Therefore, the proposed design yields broadband vibration-suppression ability.

The article is organized as follows: in section 2, the mechanism of the internal coupling realized by the shunt capacitance circuit is introduced, and an expression for the equivalent coupling stiffness is derived. The working principle of the proposed piezoelectric metamaterial beam is explained, and the stability of the system is analysed. In section 3, the analytical model of the proposed piezoelectric metamaterial beam is developed and the dispersion relation is derived under the assumption of being periodically infinitely long. A parametric study is then performed to investigate the effect of the shunt capacitance circuit technique-induced coupling on the band gaps. Subsequently, in section 4, a finitely long model is also developed, and the analytical expression of the transmittance is obtained. The predicted band gaps correspond to suppression regions in the transmittance diagrams. The effect of the coupling caused by the shunt capacitance circuit technique on the transmittance is explained using the complex band structures. Finally, in section 6, to verify the analytical solutions, an equivalent finite-element (FE) model is developed using the commercial software COMSOL. The broadband suppression ability of the proposed piezoelectric metamaterial beam is established by the FE analysis.

2. Shunt capacitance circuit technique

In this section, we use the 2-degree-of-freedom (2DOF) oscillating system (as shown in Figure 1) to explain the mechanism of the shunt capacitance circuit technique. Figure 1 shows two types of connection of the shunt circuit, that is, forward connection and reverse connection. The poling orientations of the left- and right-hand side piezoelectric transducers made of Lead zirconate titanate (PZT) ceramics are assumed to be in the same direction (i.e. from the bottom electrode to the top electrode). For the forward connection configuration, the top/bottom surfaces of the left-side PZT are connected to the top/bottom surfaces of the right-side counterpart. For the reverse connection configuration, the top/bottom surfaces of the two PZTs are reversely connected. For both configurations, a negative capacitor C_n is connected to the two PZTs in parallel.

The derivation processes of the two configurations are the same, and the conclusions are similar. The circuit connection difference between the two

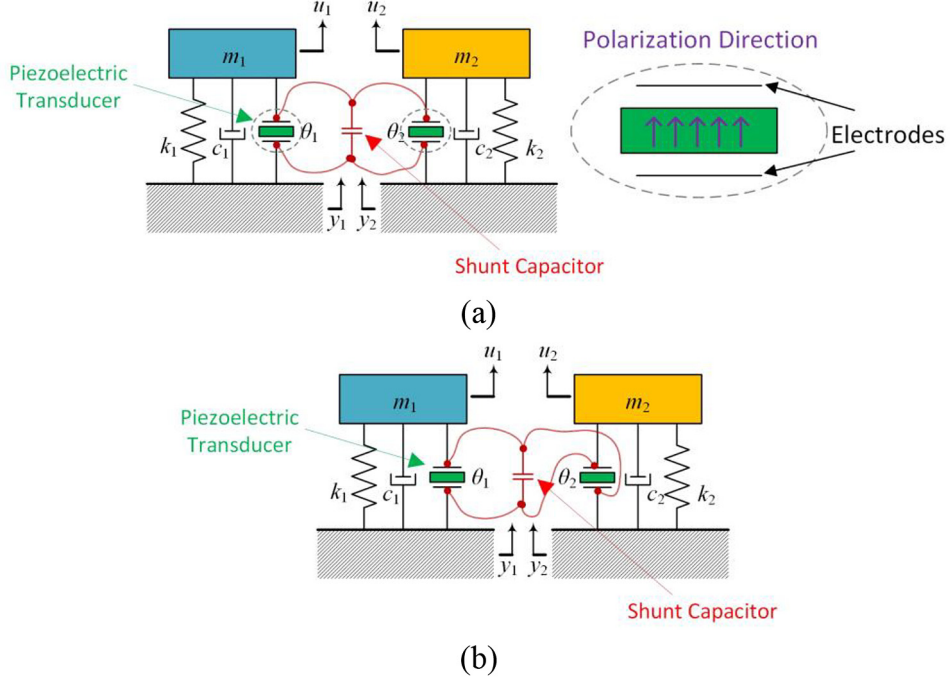


Figure 1. Schematics of 2DOF oscillating systems with negative capacitance shunted PZTs: (a) forward connection and (b) reverse connection configurations.

configurations will only result in an opposite sign in the final expression of the equivalent coupling stiffness. Indeed, one can realize the same functionality by either the forward or the reverse connection configurations with different capacitance tuning strategies. The following study only concentrates on the reverse connection configuration, as when there is no external capacitance, it behaves like a normal spring with positive stiffness which is easier to interpret as an equivalent mechanical system. The governing equations of motions of the two oscillators in the mechanical domain can be written as

$$\begin{cases} m_1 \ddot{u}_1(t) + c_1 \dot{u}_1(t) + k_1 u_1(t) + \theta_1 v_{p1}(t) = -m_1 \ddot{y}_1(t) \\ m_2 \ddot{u}_2(t) + c_2 \dot{u}_2(t) + k_2 u_2(t) + \theta_2 v_{p2}(t) = -m_2 \ddot{y}_2(t) \end{cases} \quad (1)$$

where m_1 and m_2 are the masses of the left- and right-hand side oscillators, respectively. k_1 and k_2 are the stiffness constants. c_1 and c_2 are the damping coefficients. $u_1(t)$ and $u_2(t)$ are the relative displacements of the two oscillators with respect to the host structure. θ_1 and θ_2 are the electromechanical coupling coefficients. $v_{p1}(t)$ and $v_{p2}(t)$ are the voltages across the two PZTs, respectively. $y_1(t)$ and $y_2(t)$ are the base excitation displacements for the left-hand-side and the right-hand-side oscillators, respectively. The electrical domain governing equations of the two PZTs are

$$\begin{cases} i_{p1}(t) + C_{p1} \dot{v}_{p1}(t) - \theta_1 \dot{u}_1(t) = 0 \\ i_{p2}(t) + C_{p2} \dot{v}_{p2}(t) - \theta_2 \dot{u}_2(t) = 0 \end{cases} \quad (2)$$

where C_{p1} and C_{p2} are the clamped capacitances of the two piezoelectric transducers. $i_{p1}(t)$ and $i_{p2}(t)$ are the currents flowing out of the two piezoelectric transducers. As the two PZTs are reversely connected, the voltages across the two PZTs have the same magnitudes but opposite signs. In addition, considering the relationship between the voltage across the parallel-connected capacitance C_n and the total current flowing into C_n yields

$$v_{p1}(t) = -v_{p2}(t) = \frac{\int (i_{p1}(t) - i_{p2}(t)) dt}{C_n} \quad (3)$$

2.1. Synthetic NC

The NC can be realized by the synthetic circuit (Ji et al., 2011) as shown in Figure 2. The operational amplifier (op-amp) that constitutes the synthetic circuit plays the key role for the realization of the NC. Based on the characteristics of an ideal op-amp, one can derive that the equivalent capacitance of this synthetic circuit equals to

$$C_{Synthetic} = -\frac{R_2}{R_1} C_{Real} \quad (4)$$

It can be seen that the equivalent capacitance is dependent on the ratio of R_2/R_1 , which enables the ease of tuning the equivalent capacitance value. In the physical implementation, due to the non-idealities of

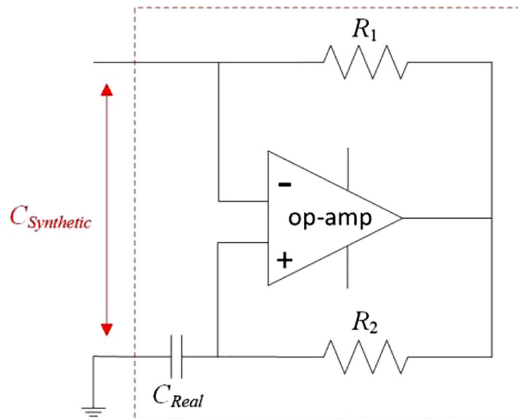


Figure 2. Synthetic circuit for realizing negative capacitance.

practical op-amps, the synthesis of op-amp circuit would unavoidably introduce undesired noise and additional parasitic elements. Fortunately, the excessive noise and additional parasitic elements besides the NC are usually negligible in the shunt circuits. First, the excessive noise from the circuit is negligible compared to the output of the shunts. For example, one of the commonly adopted op-amps for piezoelectric transducers, OPA445 (2008), has voltage noise of $15 - 20 \text{ nV}/\sqrt{\text{Hz}}$ in the frequency range of 100 Hz–100 kHz. Since the outputs of the NC shunt circuits are in the level of several volts, the noise from the op-amp is indeed negligible. Second, in practical applications, only minor resistive load besides the NC would be included in the shunt synthetic circuit (Zhu et al., 2016). The theoretical NC circuit can usually be reasonably deemed as a pure capacitive one without additional parasitic elements (De Marneffe and Preumont, 2008; Ji et al., 2011; Tang and Wang, 2001). In other words, no additional parasitic elements besides the NC need to be taken into account in the theoretical modelling and simulations of the NC synthetic circuit.

2.2. Equivalent circuit representation

Using the mechanical-electrical coupled analogies, the 2DOF oscillating system with PZTs can be represented by an equivalent electrical system as shown in Figure 3. The mechanical parameters are correspondingly converted into the electrical parameters as follows

$$\begin{aligned} L_1 &= \frac{m_1}{\theta_1^2}, \quad L_2 = \frac{m_2}{\theta_2^2}, \quad R_1 = \frac{c_1}{\theta_1^2}, \quad R_2 = \frac{c_2}{\theta_2^2} \\ C_1 &= \frac{\theta_1^2}{k_1}, \quad C_2 = \frac{\theta_2^2}{k_2}, \quad V_1 = -\frac{m_1}{\theta_1} \ddot{\theta}_1(t), \quad V_2 = -\frac{m_2}{\theta_2} \ddot{\theta}_2(t) \\ i_1(t) &= \theta_1 \dot{\theta}_1(t), \quad i_2(t) = \theta_2 \dot{\theta}_2(t) \end{aligned} \quad (5)$$

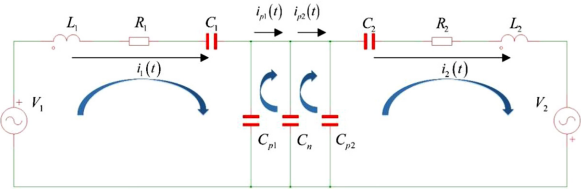


Figure 3. Equivalent circuit representation of the 2DOF oscillating system with capacitance shunting circuit.

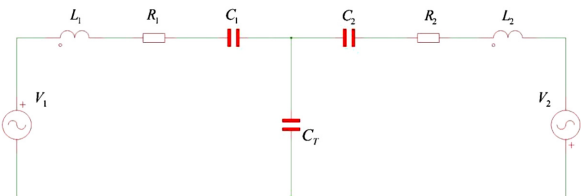


Figure 4. Simplified equivalent circuit representation of the 2DOF oscillation system with capacitance shunting circuit.

It should be noted that C_{p1} , C_{p2} , and C_n are connected in parallel. Consequently, we can replace C_{p1} , C_{p2} , and C_n by an equivalent capacitance C_T . After the replacement, the electrical system, shown in Figure 3, can be simplified into a system shown in Figure 4. A typical definition of capacitance is the ratio of the change in the electric charge to the corresponding change in the electric potential. According to this definition, when the current flows out of the capacitor, if $C_T > 0$, the voltage across the capacitor decreases; if $C_T < 0$, the voltage across the capacitor increases. Recalling the electrical-mechanical analogies (i.e. current \leftrightarrow velocity; charge \leftrightarrow displacement; and voltage \leftrightarrow force), the path consisting of $L_1-R_1-C_1$ and the path consisting of $L_2-R_2-C_2$ represent the two oscillators $m_1-c_1-k_1$ and $m_2-c_2-k_2$, respectively. Since C_T is in the parallel branch, the voltage across C_T represents the interaction force between the two oscillators. The current flowing through C_T equals to the difference between the currents in the path consisting of $L_1-R_1-C_1$ and the path consisting of $L_2-R_2-C_2$. Thus, it represents the velocity difference between the two oscillators. Moreover, the charge variation in C_T represents the displacement difference between the two oscillators. Therefore, one can easily understand that the capacitor in the electrical system can be regarded as a spring coupling the motions of the two oscillators in the mechanical domain. In addition, as the value of C_T governs the relation between the variation of the voltage across it and the variation of the current flowing through it, it can be speculated that when $C_T > 0$, the shunted PZTs would play the role as a coupling spring with a positive stiffness between the two oscillators; when $C_T < 0$, the equivalent coupling spring has a negative stiffness.

2.3. Equivalent coupling spring

In this section, the detailed mathematical derivation is presented to prove that the shunted PZTs can equiva-

$$\omega^2 = \frac{[(K + k_2)m_1 + (K + k_1)m_2] \pm \sqrt{[(K + k_2)m_1 + (K + k_1)m_2]^2 - 4m_1m_2[(k_1 + k_2)K + k_1k_2]}}{2m_1m_2} \quad (11)$$

lently play the role as a spring that couples the motions of the oscillators.

Differentiating equation (3) with respect to time gives

$$\dot{v}_{p1}(t) = -\dot{v}_{p2}(t) = \frac{(i_{p1}(t) - i_{p2}(t))}{C_n} \quad (6)$$

Substituting equation (6) into equation (2) provides the expressions of $i_{p1}(t)$ and $i_{p2}(t)$ in terms of $u_1(t)$ and $u_2(t)$

$$\begin{cases} i_{p1}(t) = \frac{C_n(C_n + C_{p2})\theta_1\dot{u}_1(t) + C_nC_{p1}\theta_2\dot{u}_2(t)}{(C_n + C_{p1})(C_n + C_{p2}) - C_{p1}C_{p2}} \\ i_{p2}(t) = \frac{C_nC_{p2}\theta_1\dot{u}_1(t) + C_n(C_n + C_{p1})\theta_2\dot{u}_2(t)}{(C_n + C_{p1})(C_n + C_{p2}) - C_{p1}C_{p2}} \end{cases} \quad (7)$$

Substituting equation (7) into equation (6) and then integrating it with respect to time gives

$$v_{p1}(t) = -v_{p2}(t) = \frac{\theta_1u_1(t) - \theta_2u_2(t)}{(C_{p1} + C_{p2} + C_n)} \quad (8)$$

After eliminating $v_{p1}(t)$ and $v_{p2}(t)$ by substituting equation (8) into equation (1), one obtains

$$\begin{cases} m_1\ddot{u}_1(t) + c_1\dot{u}_1(t) + k_1^*u_1(t) + K(u_1(t) - u_2(t)) = -m_1\ddot{y}_1(t) \\ m_2\ddot{u}_2(t) + c_2\dot{u}_2(t) + k_2^*u_2(t) + K(u_2(t) - u_1(t)) = -m_2\ddot{y}_2(t) \end{cases} \quad (9)$$

where $k_1^* = k_1 + ((\theta_1(\theta_1 - \theta_2))/(C_{p1} + C_{p2} + C_n))$, $k_2^* = k_2 + ((\theta_2(\theta_2 - \theta_1))/(C_{p1} + C_{p2} + C_n))$, and $K = \theta_1\theta_2/(C_{p1} + C_{p2} + C_n)$.

As speculated, it can be noted that shunted PZTs act as an equivalent spring that couples the motions of the two oscillators. Moreover, the shunted PZTs can also modify the effective stiffness of the two oscillators (i.e. $k_1 \rightarrow k_1^*$ or $k_2 \rightarrow k_2^*$ through the adjustment of C_n). It is worth noting that under a specific condition when $\theta_1 = \theta_2$, the shunted PZTs do not affect the effective stiffnesses of the two oscillators anymore, that is, $k_1^* = k_1$ and $k_2^* = k_2$. For the sake of simplicity to compute the eigenvalues of the 2DOF system, by dropping the damping and excitation terms, equation (9) becomes

$$\begin{cases} m_1\ddot{u}_1(t) + k_1u_1(t) + K(u_1(t) - u_2(t)) = 0 \\ m_2\ddot{u}_2(t) + k_2u_2(t) + K(u_2(t) - u_1(t)) = 0 \end{cases} \quad (10)$$

One can derive the natural frequencies of this system as

Hu et al. (2018b) proposed an internally coupled metamaterial beam that can produce an additional band gap. However, it is difficult to produce the coupling spring mechanically. It is demonstrated that the coupling of piezoelectric transducers through the shunt capacitance circuit can play the role of a spring that couples the motions of the associated oscillators. The piezoelectric coupling through circuit connection should be fairly easy to achieve in practice. Therefore, by taking advantage of the shunt capacitance circuit technique, a piezoelectric metamaterial beam with capacitance shunting is proposed and investigated in this section. It is worth mentioning that the equivalent coupling spring implemented by the shunt capacitance circuit relates the motions of the two oscillators through their relative displacements of the base, that is, $(u_1(t) - u_2(t))$. However, the internal coupling introduced by Hu et al. (2018b) coupled the motions of the two oscillators in terms of the absolute displacements using a mechanical spring. Therefore, the internal coupling realized by shunt capacitance circuit in the present work is similar but not exactly the same as that proposed by Hu et al. (2018b).

In general, arbitrary values of the masses and stiffnesses, that is, m_1 , k_1 and m_2 , k_2 of the two resonators could be taken. However, since local resonators in metamaterials are assumed to be uniform in dimensions, that is, of the same mass and stiffness, herein-after we focus on a specific case with $m_1 = m_2$ and $k_1 = k_2$. The natural frequencies presented in equation (11) can be simplified as

$$\begin{cases} \omega_1 = \omega_n \\ \omega_2 = \omega_n\sqrt{2\varepsilon + 1} \end{cases} \quad (12)$$

where $\omega_n = \sqrt{k_1/m_1}$ and $\varepsilon = K/k$ is the dimensionless stiffness of the equivalent coupling spring. It can be noted that the coupled system has two natural frequencies, as it has 2DOF and also one natural frequency is independent of the internal coupling spring stiffness. Moreover, the relation of the two natural frequencies can be summarized as

$$\begin{cases} \omega_2 \geq \omega_1 & \varepsilon \geq 0 \\ \omega_2 < \omega_1 & 0 > \varepsilon > -0.5 \end{cases} \quad (13)$$

It is known that the local resonance of resonators generate the band gaps in such an elastic metamaterial. Therefore, by coupling two neighbouring resonators,

one can roughly expect two resonant frequencies that yields additional band gaps. In fact, the coupled resonators are located at different positions of the beam, and the dynamics of the host structure may further influence the dispersion behaviours. As will be demonstrated in the following section, more than two band gaps will be generated in the proposed metamaterial beam.

2.4. Stability analysis

It is noteworthy that when the shunt capacitor is negative, which is a positive feedback system built upon op-amp circuits, the system may loss stability with improper parameter selection. The stability of the coupled dual-resonator system is analysed in this section using Jacobi's matrix. The governing equations of the system are first transformed into Jacobi's matrix. The system is deemed stable when all of the eigenvalues of the matrix have negative real part. By introducing the following definition

$$\begin{cases} x_1 = u_1 \\ x_2 = \dot{u}_1 \\ x_3 = u_2 \\ x_4 = \dot{u}_2 \end{cases} \quad (14)$$

One can rewrite equation (10) in the form as

$$\dot{\mathbf{x}} = \mathbf{X}(\mathbf{x}) \Rightarrow \begin{cases} \dot{x}_1 = x_2 \\ \dot{x}_2 = -\left(\frac{k_1}{m_1} + \frac{K}{m_1}\right)x_1 + \frac{K}{m_1}x_3 \\ \dot{x}_3 = x_4 \\ \dot{x}_4 = \frac{K}{m_1}x_1 - \left(\frac{k}{m_1} + \frac{K}{m_1}\right)x_3 \end{cases} \quad (15)$$

The Jacobi's matrix of A is then obtained as

$$\mathbf{A} = \begin{bmatrix} 0 & 1 & 0 & 0 \\ -\left(\frac{k_1}{m_1} + \frac{K}{m_1}\right) & 0 & \frac{K}{m_1} & 0 \\ 0 & 0 & 0 & 1 \\ \frac{K}{m_1} & 0 & -\left(\frac{k}{m_1} + \frac{K}{m_1}\right) & 0 \end{bmatrix} \quad (16)$$

The four eigenvalues of the matrix are

$$\begin{aligned} \lambda_1 &= \sqrt{-\frac{k_1}{m_1}}, \lambda_3 = \sqrt{-\frac{(k_1 + 2K)}{m_1}} \\ \lambda_2 &= -\sqrt{-\frac{k_1}{m_1}}, \lambda_4 = -\sqrt{-\frac{(k_1 + 2K)}{m_1}} \end{aligned} \quad (17)$$

It can be seen that λ_1 and λ_2 must be pure imaginary numbers. λ_4 must be a pure imaginary number or a negative real number. The stability of this system is dependent on the value of λ_3 . When $K < -0.5k_1$, λ_3 is a positive real number, which means that the system is unstable. When $K > -0.5k_1$, λ_3 is a pure imaginary number, which indicates that the system is stable. Therefore, by introducing a dimensionless parameter to describe the introduced internal coupling stiffness as aforementioned in equation (12), ε should satisfy the following condition to ensure the stability of this system

$$\varepsilon > -0.5 \quad (18)$$

From the perspective of tuning the circuit parameter, the value of the NC should satisfy the following criterion

$$C_n > -\left(\frac{2\theta_1\theta_2}{k_1} + C_{p1} + C_{p2}\right) \quad (19)$$

3. Band structure analysis

Figure 5 shows the infinitely long model of the proposed piezoelectric metamaterial beam. The local resonators are periodically placed on the host beam with a constant spacing of d . Each local resonator consists of a mass m_1 and a linear spring of stiffness k_1 and is embedded within a piezoelectric element. The two neighbouring piezoelectric elements are electrically connected through the aforementioned shunt capacitance circuit. By tuning the shunt capacitance, the neighbouring two local resonators can be equivalently coupled through a linear spring with a positive or negative stiffness K . For simplicity, in the following calculation, we directly develop the model with internal coupling represented by the coupling spring K . It should be mentioned that the stability of the 2DOF oscillating system has already been analysed in the previous section. The

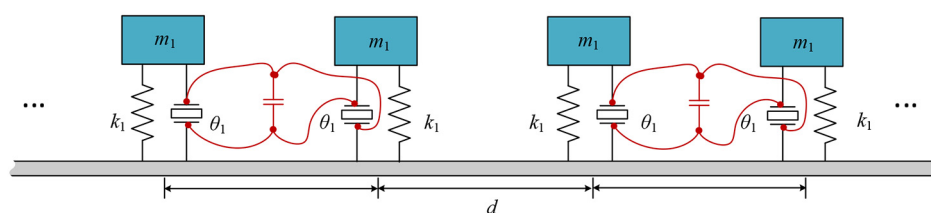


Figure 5. Infinitely long model of the piezoelectric metamaterial beam with negative capacitance shunting circuit.

2DOF system can be regarded as one of the basic components that constitutes the unit cell of the lattice

$$\begin{cases} W_j^l(x) = \left[A_j^l \cos(\beta(x - j2d)) + B_j^l \sin(\beta(x - j2d)) \right. \\ \quad \left. + C_j^l \cosh(\beta(x - j2d)) + D_j^l \sinh(\beta(x - j2d)) \right] \\ W_j^r(x) = \left[A_j^r \cos(\beta(x - j2d - d)) + B_j^r \sin(\beta(x - j2d - d)) \right. \\ \quad \left. + C_j^r \cosh(\beta(x - j2d - d)) + D_j^r \sinh(\beta(x - j2d - d)) \right] \end{cases} \quad (22)$$

vibration amplitudes of the left and right subsections of the host beam in the j th cell are assumed to be

$$\begin{cases} m_1 \ddot{u}_j^l(t) + k_1(u_j^l(t) - w_j^l(j2d, t)) + K((u_j^l(t) - w_j^l(j2d, t)) - (u_j^r(t) - w_j^r(j2d + d, t))) = 0 \\ m_1 \ddot{u}_j^r(t) + k_1(u_j^r(t) - w_j^r(j2d + d, t)) + K((u_j^r(t) - w_j^r(j2d + d, t)) - (u_j^l(t) - w_j^l(j2d, t))) = 0 \end{cases} \quad (23)$$

structure. The other component is the beam section. Only the 2DOF system component comprises the negative item which is prone to cause instability. Therefore, it can be anticipated that as long as the stabilities of the both components are ensured, the stability of the assembled system can be guaranteed. Moreover, it should be noted that the stability of the 2DOF system can always be ensured as long as the stability criterion is satisfied, regardless of the base excitations of both DOFs. After the implementation of the 2DOF system onto the host beam, the two resonators get an additional constraint on their relative base excitations, since their bases, that is, their connection points, are bonded on the same beam. Hence, due to this additional constraint condition, the 2DOF system is in fact less prone to lose the stability. In other words, the derived stability criterion for the 2DOF system must be a sufficient condition for ensuring the stability of the assembled metamaterial beam system.

Using Euler–Bernoulli beam theory, the governing equation of the host beam is given by

$$EI \frac{\partial^4 w(x, t)}{\partial x^4} + \rho A_{cs} \frac{\partial^2 w(x, t)}{\partial t^2} = 0 \quad (20)$$

where EI , ρ , and A_{cs} are the bending stiffness, mass density, and cross-section area of the host beam, respectively; $w(x, t)$ is the transverse displacement of the host beam. The solution of $w(x, t)$ is expressed in the form $w(x, t) = W(x)e^{i\omega t}$, where $W(x)$ is the vibration amplitude of the beam, and ω is the angular frequency and $i = \sqrt{-1}$ is the imaginary number. The general solution of $W(x)$ is

$$W(x) = A \cos(\beta x) + B \sin(\beta x) + C \cosh(\beta x) + D \sinh(\beta x) \quad (21)$$

where $\beta^4 = \rho A_{cs} \omega^2 / EI$. Each unit cell of the metamaterial beam consists of two subsections of the host beam and two local resonators. Therefore, the

The equations of motions for the two local resonators in the j th cell are

where $u_j^l(t)$ and $u_j^r(t)$ are the absolute displacements of the local resonators. The reaction forces of the local resonators in the j th cell acting onto the host beam can be calculated as

$$\begin{cases} F_j^l = k(W_j^l(j2d) - U_j^l) \\ F_j^r = k(W_j^r(j2d + d) - U_j^r) \end{cases} \quad (24)$$

Solving equation (23) to represent the displacement magnitudes of local resonators U_j^l and U_j^r in terms of W_j^l and W_j^r , and substituting them into equation (24) gives

$$\begin{cases} F_j^l = aW_j^l(j2d) - bW_j^r(j2d + d) \\ F_j^r = -bW_j^l(j2d) + aW_j^r(j2d + d) \end{cases} \quad (25)$$

where
 $a = (k_1 m_1 \omega^2 (m_1 \omega^2 - k_1 - K) / ((k_1 + K - \omega^2 m_1)^2 - K^2))$
and $b = k_1 K m_1 \omega^2 / ((k_1 + K - \omega^2 m_1)^2 - K^2)$.

Considering the continuity conditions (i.e. deflection, slope, bending moment, and shear force) at the intersection between the left and right subsections of the host beam in the $(j-1)$ th cell, one obtains

$$\mathbf{K} \Psi_{j-1}^r = \mathbf{H} \Psi_{j-1}^l \quad (26)$$

where $\Psi_{j-1}^r = [A_{j-1}^r \ B_{j-1}^r \ C_{j-1}^r \ D_{j-1}^r]^T$ and $\Psi_{j-1}^l = [A_{j-1}^l \ B_{j-1}^l \ C_{j-1}^l \ D_{j-1}^l]^T$

$$\mathbf{K} = \begin{bmatrix} 1 & 0 & 1 & 0 \\ 0 & 1 & 0 & 1 \\ -1 & 0 & 1 & 0 \\ \frac{a}{\beta^3 EI} & -1 & \frac{a}{\beta^3 EI} & 1 \end{bmatrix}$$

$$\mathbf{H} = \begin{bmatrix} \cos(\beta d) & \sin(\beta d) & \cosh(\beta d) & \sinh(\beta d) \\ -\sin(\beta d) & \cos(\beta d) & \sinh(\beta d) & \cosh(\beta d) \\ -\cos(\beta d) & -\sin(\beta d) & \cosh(\beta d) & \sinh(\beta d) \\ \left(\sin(\beta d) + \frac{b}{\beta^3 EI}\right) & -\cos(\beta d) & \left(\sinh(\beta d) + \frac{b}{\beta^3 EI}\right) & \cosh(\beta d) \end{bmatrix}$$

Similarly, the continuity conditions at the intersection between the $(j-1)$ th cell and the j th cell gives

$$\mathbf{A}\Psi_j^l + \mathbf{B}\Psi_j^r = \mathbf{H}'\Psi_{j-1}^r \quad (27)$$

where $\Psi_j^l = [A_j^l \ B_j^l \ C_j^l \ D_j^l]^T$ and $\Psi_{j-1}^r = [A_{j-1}^r \ B_{j-1}^r \ C_{j-1}^r \ D_{j-1}^r]^T$

$$\mathbf{A} = \begin{bmatrix} 1 & 0 & 1 & 0 \\ 0 & 1 & 0 & 1 \\ -\frac{1}{a} & 0 & \frac{1}{a} & 0 \\ \frac{\beta^3 EI}{\beta^3 EI} & -1 & \frac{\beta^3 EI}{\beta^3 EI} & 1 \end{bmatrix}$$

$$\mathbf{B} = \begin{bmatrix} 0 & 0 & 0 & 0 \\ 0 & 0 & 0 & 0 \\ 0 & b & 0 & 0 \\ -\frac{b}{\beta^3 EI} & 0 & -\frac{b}{\beta^3 EI} & 0 \end{bmatrix}$$

$$\mathbf{H}' = \begin{bmatrix} \cos(\beta d) & \sin(\beta d) & \cosh(\beta d) & \sinh(\beta d) \\ -\sin(\beta d) & \cos(\beta d) & \sinh(\beta d) & \cosh(\beta d) \\ -\cos(\beta d) & -\sin(\beta d) & \cosh(\beta d) & \sinh(\beta d) \\ \sin(\beta d) & -\cos(\beta d) & \sinh(\beta d) & \cosh(\beta d) \end{bmatrix}$$

Combining equations (26) and (27) and eliminating Ψ_{j-1}^r and Ψ_j^r , the transfer relation between the two neighbouring cells can be obtained as

$$\Psi_j^l = \underbrace{(\mathbf{A} + \mathbf{B}\mathbf{K}^{-1}\mathbf{H})^{-1}\mathbf{H}'(\mathbf{K})^{-1}\mathbf{H}}_{\mathbf{T}}\Psi_{j-1}^l \quad (28)$$

Using Bloch theorem, the infinite periodic condition is applied as

$$\Psi_j^l = e^{iq2d}\Psi_{j-1}^l \quad (29)$$

where q is the wavenumber. By inserting equation (28) into equation (29), we obtain a standard eigenvalue problem

$$|\mathbf{T} - e^{iq2d}\mathbf{I}| = 0 \quad (30)$$

where \mathbf{T} is the transfer matrix, and \mathbf{I} is the fourth-order square unit matrix.

Figure 6 shows the real part of the complex band structures of the proposed metamaterial beam with different equivalent coupling stiffnesses -434.9 , 1304.7 , 2174.5 , and 3044.3 N/m (the corresponding ε are -0.05 , -0.15 , -0.25 , and -0.35). The geometrical and material parameters used for the example case study are listed in Table 1. The x -axis denotes the normalized wave number ($q^* = 2dq/\pi$). The band gap of the metamaterial beam without shunt capacitance circuit ($\varepsilon = 0$) is also shown for comparison. It is worth mentioning that the real parts of the complex wavenumbers inside the band gaps are not plotted in Figure 6 to clearly show the band gap regions. It can be observed that the introduction of shunt capacitance circuit opens

Table I. Geometric and material parameters for the case study.

| Parameters | Values |
|-----------------------------------|----------------------------------|
| Beam cross-section area, A_{cs} | $0.020 \times 0.004 \text{ m}^2$ |
| Beam mass density, ρ | 7850 kg/m^3 |
| Young's modulus, E | $200 \times 10^9 \text{ Pa}$ |
| Adjacent spacing, d | 0.150 m |
| Local resonator mass, m_1 | 0.0272 kg |
| Local resonator stiffness, k_1 | $8.698 \times 10^3 \text{ N/m}$ |

two more band gaps in the metamaterial beam in the frequency range of interest. In addition, with the increase of $|\varepsilon|$, the first band gap shows a clear trend of moving towards the lower frequency range. As analysed in section 2.2, one of the natural frequency of the standalone 2DOF oscillating sub-system is $\omega_n\sqrt{2\varepsilon + 1}$ (equation (17)). When $\varepsilon < 0$ (i.e. $\omega_n\sqrt{2\varepsilon + 1} < \omega_n$), this natural frequency qualitatively predicts the location of the first band gap. Focusing on the value of ε being in the negative regime, with the increase of $|\varepsilon|$, $\omega_n\sqrt{2\varepsilon + 1}$ apparently decreases, thus the first band gap moves towards the lower frequency range.

For the second and third band gaps, their lower bounds also move towards a lower frequency, but the upper bounds remain insensitive to the variation of ε . Moreover, the band gap width of the conventional band gap has been broadened due to the presence shunt capacitance circuit. It is well known that the larger inertial force could enhance the width of the band gap (e.g. with a larger mass in the local resonator (Sun et al., 2010)). As explained in section 2.2, the presence of the shunt capacitance circuit is equivalent to a coupling spring. In this research, the coupling spring is carefully tuned to exhibit negative stiffness through the manipulation with the shunt capacitance circuit. In the case of our proposed metamaterial system, the negative stiffness spring gives the system the tendency for larger dynamic motion (the extreme case is the loss of stability); therefore, the inertia force will be enhanced. The internal shear force of the host beam is cancelled by the larger inertia forces of the local resonators over a wider frequency range (Sun et al., 2010), which will eventually widen the band gap, similar to the effect using larger masses in the local resonators.

Figure 7 shows the imaginary part of the complex band structure that reveals the suppression performance in the band gaps. The suppression ability is reflected by the absolute value of the imaginary part. It can be found that the second band gap demonstrates the best suppression ability as compared to the other two band gaps. Comparing the four figures (Figure 7(a) to (d)), the suppression abilities of the first and the third band gaps increase with the increase of $|\varepsilon|$. However, the suppression ability of the second band

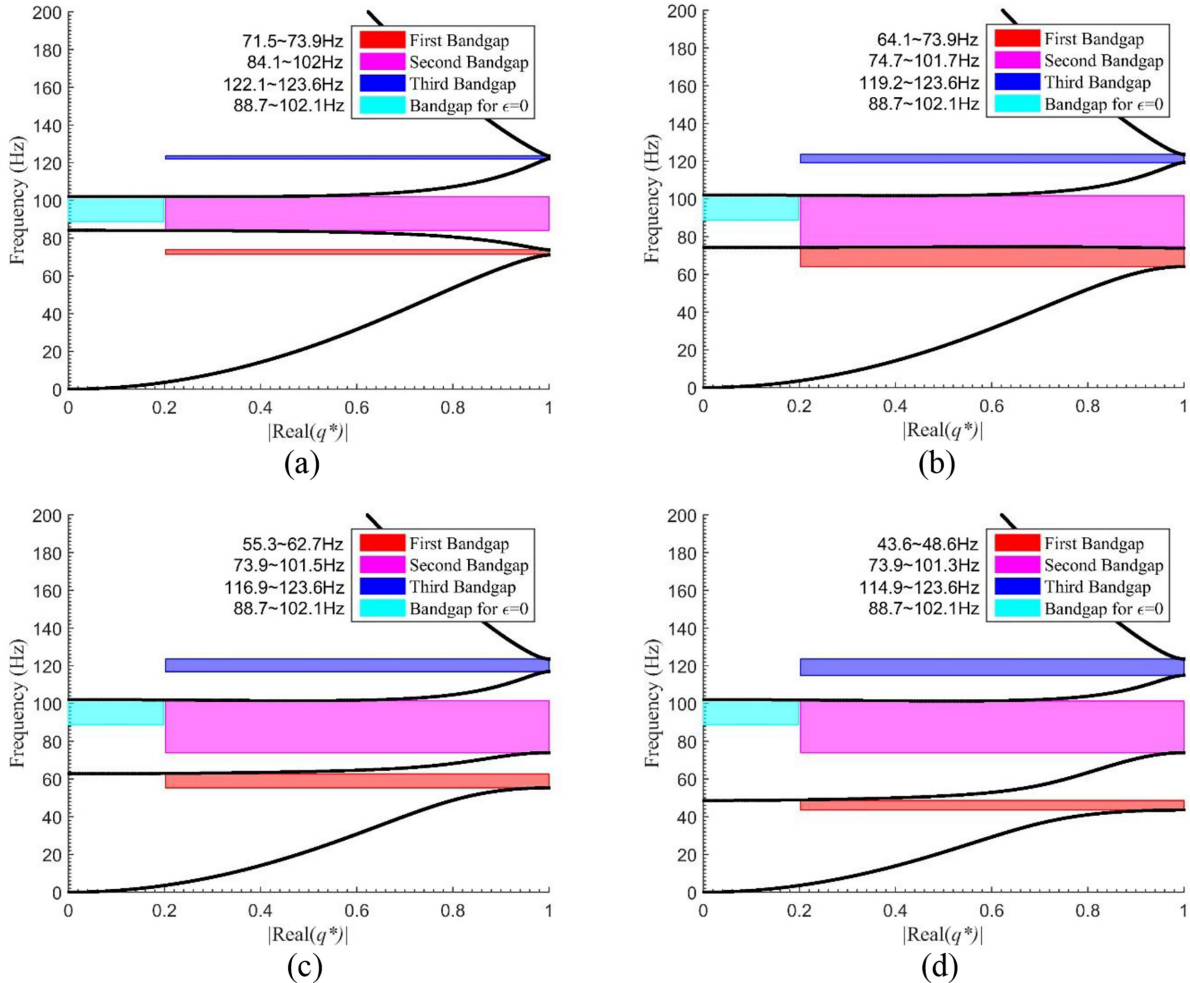


Figure 6. Real part of complex band structures of the proposed piezoelectric metamaterial beams with different effective coupling spring stiffnesses: (a) $\varepsilon = -0.05$, (b) $\varepsilon = -0.15$, (c) $\varepsilon = -0.25$, and (d) $\varepsilon = -0.35$.

gap decreases accordingly. In addition, it can be noted that when $|\varepsilon|$ is very small, the suppression abilities of the first and the third band gaps are very weak (Figure 7(a)). Increasing $|\varepsilon|$ could improve the wave isolation capability for the first band gap. In addition, the third band gap could nearly be impossible to be changed for achieving a significant contribution to vibration suppression. Therefore, it can be anticipated that for a realistic metamaterial model consisting of limited number of unit cells, it might be difficult for the third band gap to appear as an effective suppression region in the transmittance.

To understand the formation mechanism of band gaps, the displacement distribution of the responses of the proposed metamaterial with $\varepsilon = -0.35$ is conducted to reveal the dynamic interactions between the host beam and the local resonators. For ideal infinitely long models, the vibration mode of the metamaterial beam within the band gaps is like a plain beam at the static equilibrium, which means that waves are restricted for propagation. Therefore, a semi-infinitely long model is

investigated. The metamaterial beam is under the free-boundary condition at the left side and extends infinitely towards the right side. The displacement distributions of the responses are normalized by the vibration amplitude of the left side of the semi-infinitely long model. Figure 8 shows the displacement distribution of responses of the metamaterial beam for points A, B, C, and D, which are labelled respectively in the band structure of Figure 7. The black and red solid circles denote the local resonators.

As the four points are within band gaps, it can be noted that their displacement responses have a common feature, that is, the vibration amplitude of the host beam decays along the direction of wave propagation. It can be anticipated that since the model is assumed to be infinitely long towards the right direction, the displacement distribution of responses of the section that is farther away from the left side will be similar to a plain beam at the static equilibrium. This means the vibration energy will be attenuated along the propagation direction. For point A (Figure 8(a)), the motion of the left-

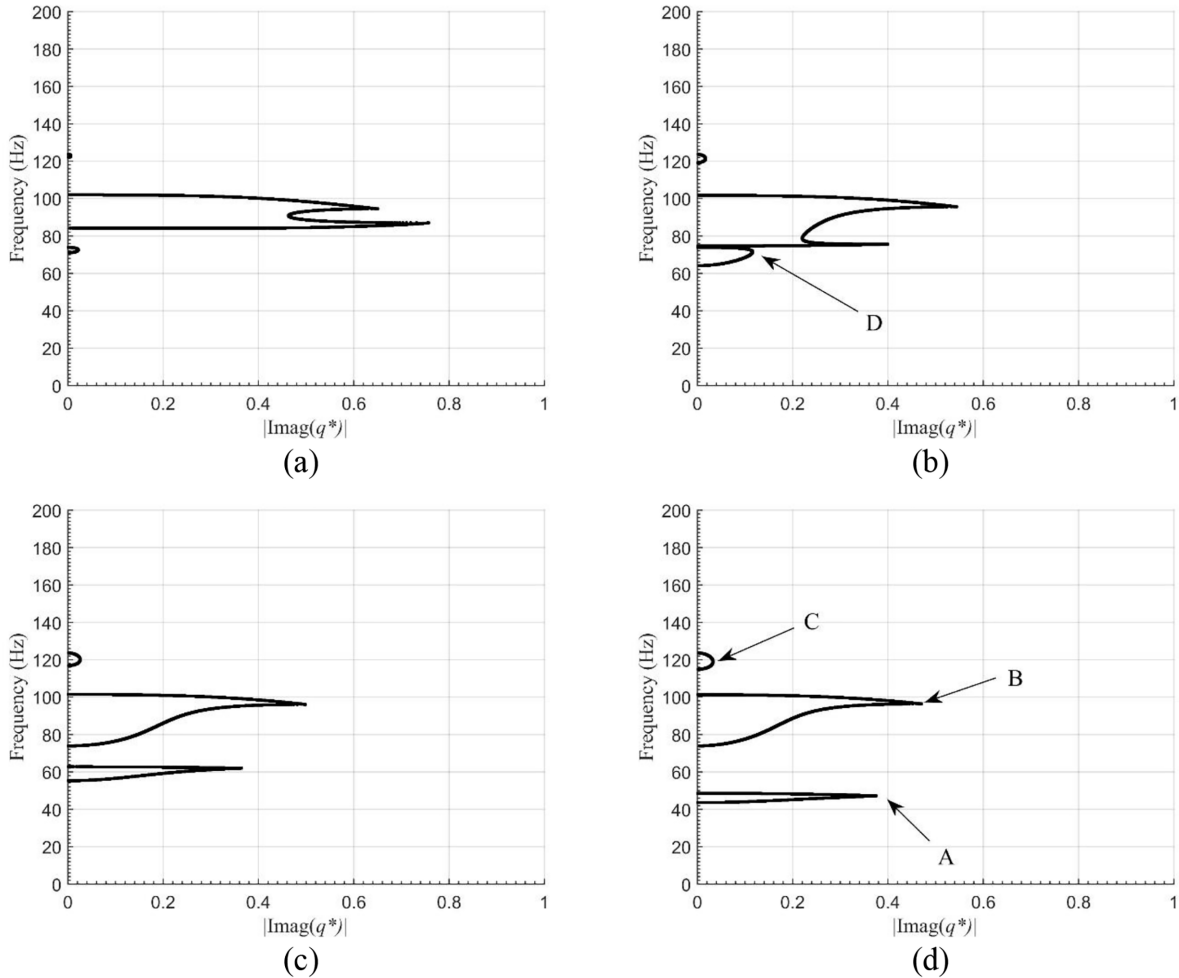


Figure 7. Imaginary part of complex band structures of the proposed piezoelectric metamaterial beams with different effective coupling spring stiffnesses: (a) $\varepsilon = -0.05$, (b) $\varepsilon = -0.15$, (c) $\varepsilon = -0.25$, and (d) $\varepsilon = -0.35$.

side resonator (black solid circle) is in phase with the motion of the host beam, that is, their motions are always in the same direction. It is the out-of-phase motion of the right-side local resonator (red solid circle) in a unit cell that counteracts with the host beam, thus generates the first band gap. Here, the out-of-phase motion means that the resonator and the point of the beam where the resonator is attached are always moving in the opposite directions. At point B, which is within the second band gap, both local resonators have out-of-phase motions. Therefore, the second band gap is opened. In addition, as both the local resonators are contributing to the generation of the second band gap, the suppression ability of the second band gap is the best. This may not be easily seen by comparing Figure 7(a) and (b), because for this case $\varepsilon = -0.35$, the first band gap has been tuned to have a similar suppression ability as the second band gap (Figure 7(d)). To give a counter-example of weak suppression ability, Figure 8(d) shows the displacement distribution of responses of the metamaterial beam for point D which corresponds to the first band gap of the case where

$\varepsilon = -0.15$. It is found that the motion shown in Figure 8(d) is similar to that shown in Figure 8(a). The left-side local resonator is in phase and the right-side one is out of phase. However, Figure 8(d) shows that the suppression ability of the first band gap for this case becomes much weaker which has already been predicted as shown in Figure 7(b). Inside the third band gap at point C, it can be found that the motion of the right-side local resonator is in phase, while the left-side one becomes out of phase. This implies that the left-side local resonator becomes the dominant factor for generating the third band gap. However, by comparing Figure 7(c) with (a) and (b), it can be seen that though this mechanism also provides the wave-suppression function, the suppression ability generated by this mechanism is much weaker as compared to the suppression abilities generated by the other two mechanisms.

4. Transmittance analysis

Figure 9 shows the finitely long model of the proposed piezoelectric metamaterial beam. The entire host beam

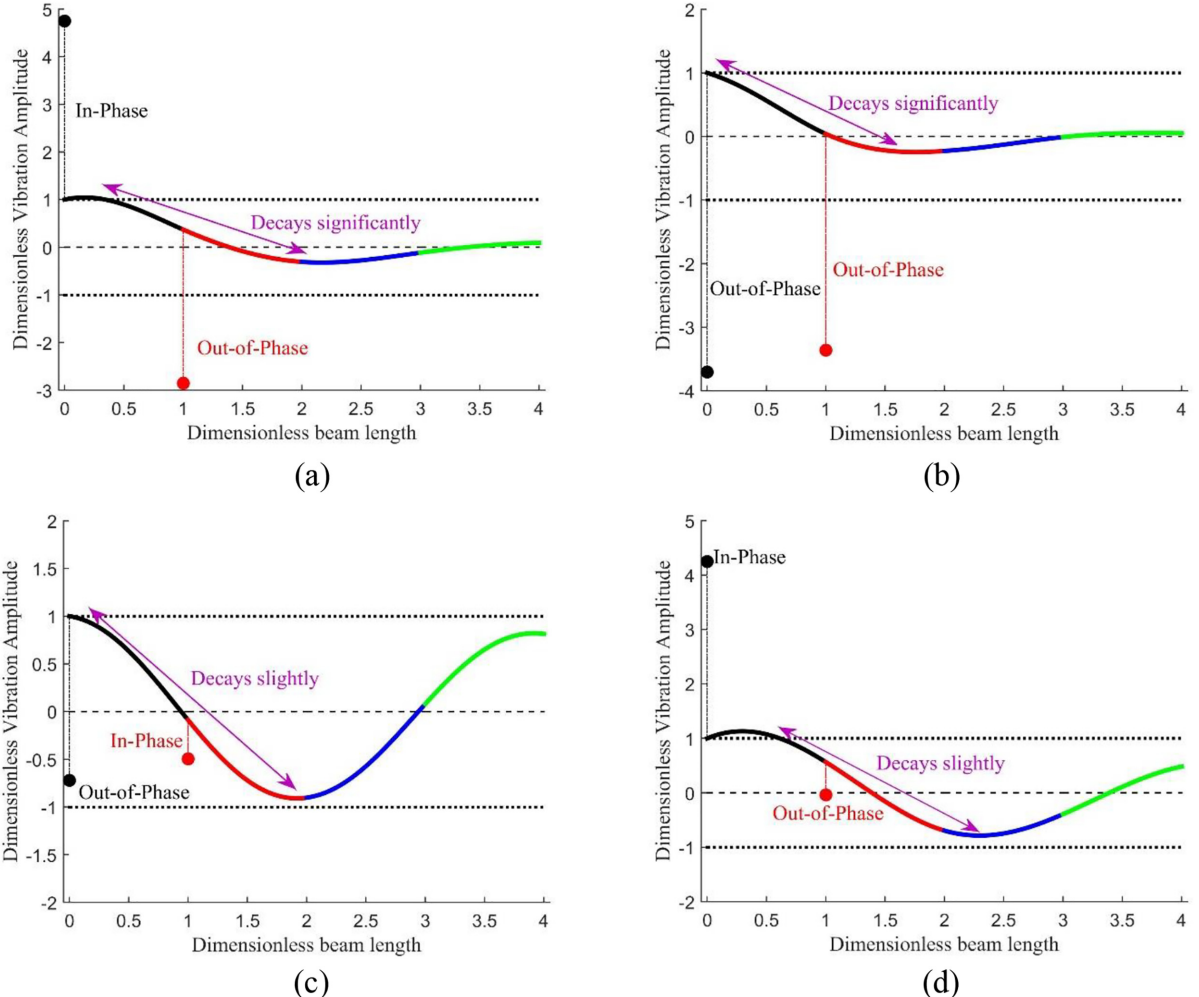


Figure 8. Mode shapes of semi-ininitely long metamaterial beam: (a), (b), (c), and (d) are for the points labelled A, B, C, and D in the band structure of Figure 7, respectively.

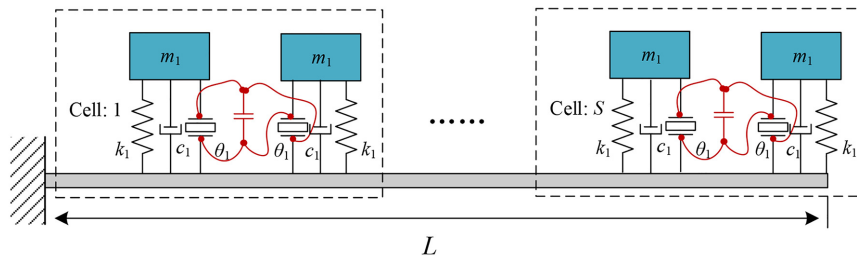


Figure 9. Finitely long model of the piezoelectric metamaterial beam with shunt capacitance circuit. In the legend, XCXR is short for X cells and X resonators.

has length of L . S pairs of uniform resonators are periodically attached onto the host beam at a constant distance of d . Each resonator is embedded with a piezoelectric element and the circuit connections have been explained in the previous section. One side of the host beam is clamped to the base, and the other side is free. The base experiences a harmonic excitation $w_b(t) = W_b e^{i\omega t}$ and the acceleration is controlled at a constant acceleration $a_{cc} = -\omega^2 W_b$. Using Euler-

Bernoulli beam theory, the governing equation of the host beam is written as

$$\begin{aligned}
 EI \frac{\partial^4 w_{rel}(x, t)}{\partial x^4} + c_s I \frac{\partial^5 w_{rel}(x, t)}{\partial x^4 \partial t} + \rho A_{cs} \frac{\partial^2 w_{rel}(x, t)}{\partial t^2} \\
 = \rho A_{cs} a_{cc} e^{i\omega t} - \sum_{j=1}^S \left[F_{bj}^l \delta(x - x_j^l) e^{i\omega t} + F_{bj}^r \delta(x - x_j^r) e^{i\omega t} \right]
 \end{aligned} \quad (31)$$

where $w_{rel}(x, t)$ is the relative transverse displacement between the beam and the base; c_s is the equivalent strain rate damping constant; F_{bj}^l and F_{bj}^r are the reaction forces exerted by the left and right resonators in the j th cell onto the beam during vibration, respectively; $\delta(x)$ is the Dirac delta function. The equations of motion for resonators are

$$\begin{cases} m_1 \ddot{\tilde{u}}_j^l(t) + c_1 \dot{\tilde{u}}_j^l(t) + k_1 \tilde{u}_j^l(t) + K(\tilde{u}_j^l(t) - \tilde{u}_j^r(t)) = -m_1 \ddot{w}(x_j^l, t) \\ m_1 \ddot{\tilde{u}}_j^r(t) + c_1 \dot{\tilde{u}}_j^r(t) + k_1 \tilde{u}_j^r(t) + K(\tilde{u}_j^r(t) - \tilde{u}_j^l(t)) = -m_1 \ddot{w}(x_j^r, t) \end{cases} \quad (32)$$

where c_1 is the damping coefficient of the local resonators. $\tilde{u}_j^l(t)$ and $\tilde{u}_j^r(t)$ are the displacements of the left and right resonators in the j th cell relative to the host beam, respectively. The absolute displacement of the resonator should add $w(x_j, t) = w_{rel}(x, t) + w_b(t)$ which is the absolute transverse displacement of the beam. K is the equivalent coupling spring stiffness due to the implementation of the shunt capacitance circuit. Using the modal superposition method, the relative displacement along the host beam can be written as

$$w_{rel}(x, t) = \sum_{k=1}^{\infty} \phi_k(x) \eta_k(t) \quad (k = 1, 2, 3, \dots) \quad (33)$$

where functions $\phi_k(x)$ are the mass normalized mode shape functions of the plain beam (i.e. without resonators) and functions $\eta_k(t)$ are the modal coordinates. Substituting equation (33) into equation (31), multiplying by $\phi_n(x)$ and integrating over the beam length from 0 to L , then using the orthogonal conditions ($\int_0^L \rho A_{cs} \phi_k(x) \phi_n(x) dx = \delta_{kn}$ and $\int_0^L EI(d^4 \phi_k(x)/dx^4) \phi_n(x) dx = \omega_k^2 \delta_{kn}$), we obtain the modal governing equation as

$$\begin{cases} f_j^l = -[c_1 \dot{\tilde{u}}_j^l(t) + k_1 \tilde{u}_j^l(t)] = -(k_1 + i\omega c_1) \alpha_1 w_{rel}(x_j^l, t) + \alpha_2 w_{rel}(x_j^r, t) + \alpha_3 w_b(t) \\ f_j^r = -[c_1 \dot{\tilde{u}}_j^r(t) + k_1 \tilde{u}_j^r(t)] = -(k_1 + i\omega c_1) \alpha_2 w_{rel}(x_j^l, t) + \alpha_1 w_{rel}(x_j^r, t) + \alpha_3 w_b(t) \end{cases} \quad (37)$$

Substituting equation (35) into equation (37) gives the expression of the force amplitude as

$$\left\{ \begin{array}{l} F_j^l = -(k_1 + i\omega c_1) \left\{ \begin{array}{l} \alpha_1 \times \sum_{k=1}^{\infty} \phi_k(x_j^l) \frac{\rho A_{cs} a_{cc} \int_0^L \phi_k(x) dx - \sum_{h=1}^S [F_h^l \phi_k(x_h^l) + F_h^r \phi_k(x_h^r)]}{\omega_k^2 - \omega^2 + 2i\zeta_k \omega_k \omega} \\ + \alpha_2 \times \sum_{k=1}^{\infty} \phi_k(x_j^r) \frac{\rho A_{cs} a_{cc} \int_0^L \phi_k(x) dx - \sum_{h=1}^S [F_h^l \phi_k(x_h^l) + F_h^r \phi_k(x_h^r)]}{\omega_k^2 - \omega^2 + 2i\zeta_k \omega_k \omega} + \alpha_3 \frac{a_{cc}}{\omega^2} \end{array} \right\} \\ F_j^r = -(k_1 + i\omega c_1) \left\{ \begin{array}{l} \alpha_2 \times \sum_{k=1}^{\infty} \phi_k(x_j^l) \frac{\rho A_{cs} a_{cc} \int_0^L \phi_k(x) dx - \sum_{h=1}^S [F_h^l \phi_k(x_h^l) + F_h^r \phi_k(x_h^r)]}{\omega_k^2 - \omega^2 + 2i\zeta_k \omega_k \omega} \\ + \alpha_1 \times \sum_{k=1}^{\infty} \phi_k(x_j^r) \frac{\rho A_{cs} a_{cc} \int_0^L \phi_k(x) dx - \sum_{h=1}^S [F_h^l \phi_k(x_h^l) + F_h^r \phi_k(x_h^r)]}{\omega_k^2 - \omega^2 + 2i\zeta_k \omega_k \omega} + \alpha_3 \frac{a_{cc}}{\omega^2} \end{array} \right\} \end{array} \right\} \quad (38)$$

Rearrange the 2S reaction force equations, that is, $F_1^l, F_2^l, \dots, F_S^l, F_1^r, F_2^r, \dots, F_S^r$

$$\begin{aligned} \ddot{\eta}_k(t) + 2\zeta_k \omega_k \dot{\eta}_k(t) + \omega_k^2 \eta_k(t) &= \rho A_{cs} a_{cc} e^{i\omega t} \\ \int_0^L \phi_k(x) dx - \sum_{j=1}^S &\left[F_j^l \phi_k(x_j^l) e^{i\omega t} + F_j^r \phi_k(x_j^r) e^{i\omega t} \right] \end{aligned} \quad (34)$$

where $\zeta_k = c_s I \omega_k / 2E$ is the mechanical damping ratio. The expression of $\eta_k(t)$ can be derived from equation (34). Substituting the derived $\eta_k(t)$ into equation (33) renders the closed-form solution of the relative displacement as

$$\begin{aligned} w_{rel}(x, t) &= \sum_{k=1}^{\infty} \phi_k(x) \\ \frac{\rho A_{cs} a_{cc} \int_0^L \phi_k(x) dx - \sum_{j=1}^S [F_j^l \phi_k(x_j^l) + F_j^r \phi_k(x_j^r)]}{\omega_k^2 - \omega^2 + 2i\zeta_k \omega_k \omega} e^{i\omega t} \end{aligned} \quad (35)$$

From equation (32), we can obtain

$$\begin{cases} \tilde{u}_j^l(t) = \alpha_1 w_{rel}(x_j^l, t) + \alpha_2 w_{rel}(x_j^r, t) + \alpha_3 w_b(t) \\ \tilde{u}_j^r(t) = \alpha_2 w_{rel}(x_j^l, t) + \alpha_1 w_{rel}(x_j^r, t) + \alpha_3 w_b(t) \end{cases} \quad (36)$$

where

$$\begin{cases} \alpha_1 = \frac{(k_1 + K - m_1 \omega^2 + i\omega c_1) \omega^2}{(k_1 + K - m_1 \omega^2 + i\omega c_1)^2 - K^2} \\ \alpha_2 = \frac{K \omega^2}{(k_1 + K - m_1 \omega^2 + i\omega c_1)^2 - K^2} \\ \alpha_3 = \alpha_1 + \alpha_2 \end{cases}$$

The reaction forces exerted by the left and right resonators in the j th cell onto the beam are expressed as

$$\mathbf{aF} = \mathbf{b} \quad (39)$$

where

$$a_{j,h} = \begin{cases} \left(\alpha_1 \times \sum_{k=1}^{\infty} \frac{\phi_k(x_j^l)\phi_k(x_h^l)}{\omega_k^2 - \omega^2 + 2i\zeta_k\omega_k\omega} + \alpha_2 \times \sum_{k=1}^{\infty} \frac{\phi_k(x_j^r)\phi_k(x_h^r)}{\omega_k^2 - \omega^2 + 2i\zeta_k\omega_k\omega} \right) & \text{for } 1 \leq j \leq S; 1 \leq h \leq S \\ \left(\alpha_1 \times \sum_{k=1}^{\infty} \frac{\phi_k(x_j^l)\phi_k(x_{(h-S)}^r)}{\omega_k^2 - \omega^2 + 2i\zeta_k\omega_k\omega} + \alpha_2 \times \sum_{k=1}^{\infty} \frac{\phi_k(x_j^r)\phi_k(x_{(h-S)}^r)}{\omega_k^2 - \omega^2 + 2i\zeta_k\omega_k\omega} \right) & \text{for } 1 \leq j \leq S; S+1 \leq h \leq 2S \\ \left(\alpha_2 \times \sum_{k=1}^{\infty} \frac{\phi_k(x_{(j-S)}^l)\phi_k(x_h^l)}{\omega_k^2 - \omega^2 + 2i\zeta_k\omega_k\omega} + \alpha_1 \times \sum_{k=1}^{\infty} \frac{\phi_k(x_{(j-S)}^r)\phi_k(x_h^r)}{\omega_k^2 - \omega^2 + 2i\zeta_k\omega_k\omega} \right) & \text{for } S+1 \leq j \leq 2S; 1 \leq h \leq S \\ \left(\alpha_2 \times \sum_{k=1}^{\infty} \frac{\phi_k(x_{(j-S)}^l)\phi_k(x_{(h-S)}^r)}{\omega_k^2 - \omega^2 + 2i\zeta_k\omega_k\omega} + \alpha_1 \times \sum_{k=1}^{\infty} \frac{\phi_k(x_{(j-S)}^r)\phi_k(x_{(h-S)}^r)}{\omega_k^2 - \omega^2 + 2i\zeta_k\omega_k\omega} \right) & \text{for } S+1 \leq j \leq 2S; S+1 \leq h \leq 2S \end{cases}$$

$$a_{j,j} = \begin{cases} \left(\alpha_1 \times \sum_{k=1}^{\infty} \frac{\phi_k(x_j^l)\phi_k(x_j^l)}{\omega_k^2 - \omega^2 + 2i\zeta_k\omega_k\omega} + \alpha_2 \times \sum_{k=1}^{\infty} \frac{\phi_k(x_j^r)\phi_k(x_j^r)}{\omega_k^2 - \omega^2 + 2i\zeta_k\omega_k\omega} - \frac{1}{(k_1 + i\omega c_1)} \right) & \text{for } 1 \leq j \leq S \\ \left(\alpha_2 \times \sum_{k=1}^{\infty} \frac{\phi_k(x_{(j-S)}^l)\phi_k(x_{(j-S)}^r)}{\omega_k^2 - \omega^2 + 2i\zeta_k\omega_k\omega} + \alpha_1 \times \sum_{k=1}^{\infty} \frac{\phi_k(x_{(j-S)}^r)\phi_k(x_{(j-S)}^r)}{\omega_k^2 - \omega^2 + 2i\zeta_k\omega_k\omega} - \frac{1}{(k_1 + i\omega c_1)} \right) & \text{for } S+1 \leq j \leq 2S \end{cases}$$

$$b_j = \begin{cases} \left(\alpha_1 \times \sum_{k=1}^{\infty} \phi_k(x_j^l) \frac{\rho A_{cs} a_{cc} \int_0^L \phi_k(x) dx}{\omega_k^2 - \omega^2 + 2i\zeta_k\omega_k\omega} + \alpha_2 \times \sum_{k=1}^{\infty} \phi_k(x_j^r) \frac{\rho A_{cs} a_{cc} \int_0^L \phi_k(x) dx}{\omega_k^2 - \omega^2 + 2i\zeta_k\omega_k\omega} + \alpha_3 \frac{a_{cc}}{\omega^2} \right) & \text{for } 1 \leq j \leq S \\ \left(\alpha_2 \times \sum_{k=1}^{\infty} \phi_k(x_{(j-S)}^l) \frac{\rho A_{cs} a_{cc} \int_0^L \phi_k(x) dx}{\omega_k^2 - \omega^2 + 2i\zeta_k\omega_k\omega} + \alpha_1 \times \sum_{k=1}^{\infty} \phi_k(x_{(j-S)}^r) \frac{\rho A_{cs} a_{cc} \int_0^L \phi_k(x) dx}{\omega_k^2 - \omega^2 + 2i\zeta_k\omega_k\omega} + \alpha_3 \frac{a_{cc}}{\omega^2} \right) & \text{for } S+1 \leq j \leq 2S \end{cases}$$

By solving equation (39), the 2S values of F_j^l and F_j^r can be calculated. Substituting them back into equation (35), the relative deflection amplitude $W_{rel}(x)$ can be obtained. The transmittance of the system is defined and calculated as

$$\tau = \frac{|W_{rel}(L) + W_b|}{|W_b|} \quad (40)$$

For the same parameters listed in Table 1, Figure 10 shows the transmittances of the corresponding finitely long models with different equivalent coupling stiffnesses -434.9 , 1304.7 , 2174.5 , and 3044.3 N/m (the corresponding ε are -0.05 , -0.15 , -0.25 , and -0.35). The additional parameters used in the calculation are as follows: the material damping ratio is 0.006 ; the resonator damping ratio is 0.006 . It is known that the transmittance including the suppression region is very sensitive to the damping (Hu et al., 2017a, 2017b). The prediction of suppression regions based on the transmittance analysis may show a deviation from the prediction of band gaps based on the band structure analysis because of the existence of a large damping. The damping ratios are selected to be relatively small but still within the reasonable range. The transmittance of the metamaterial beam without shunt capacitance

circuit (i.e. $\varepsilon = 0$) is also provided in the figures for comparison. In the transmittances, additional suppression regions appear in the frequency domain responses. This phenomenon agrees well with the above prediction from the band structure analysis. It is worth emphasizing that the band gap width of the metamaterial beam has been significantly broadened with the implement of shunt capacitance circuit. Moreover, as speculated from the complex band structures, there are only two evident suppression regions (Figure 10(b) to (c)), and the third band gap that exists in theory does not generate a practical suppression region as the suppression ability of this band gap is quite weak. Moreover, when ε is small, even the first suppression region disappears, for the same reason of the strongly decreased suppression ability. In addition, the effect of ε on the movements of the band gaps revealed by the transmittance analysis is also found to match the findings from the band structure analysis.

It is noteworthy that one may mistake the small dip (marked with a red ellipse in Figure 11(a)) before the band gap of the metamaterial beam without shunt capacitance circuit as a part of the band gap range. Actually, this small dip is not formed by the same mechanism for the generation of band gaps. Its existence is due to the damping effect and the fact that the

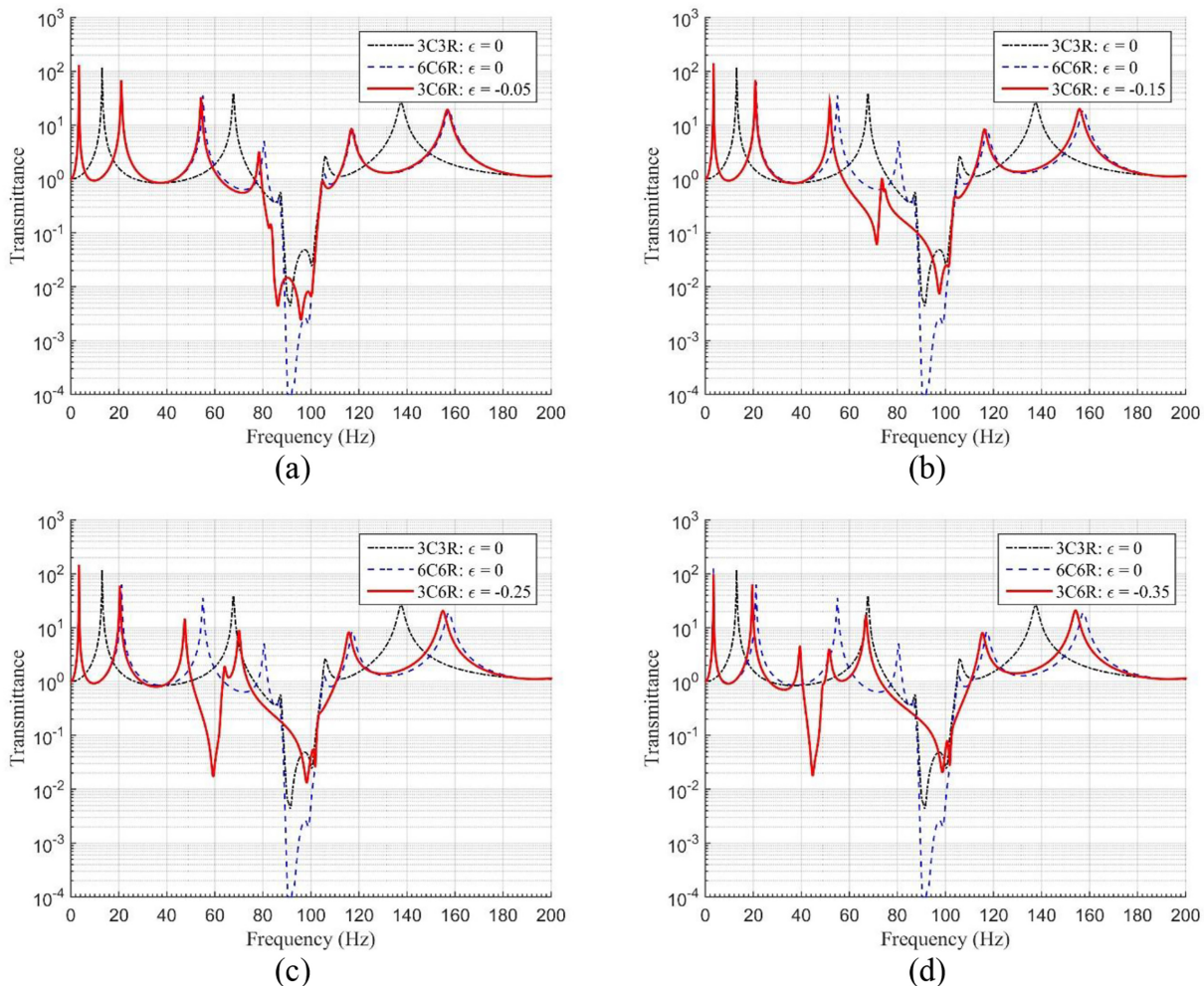


Figure 10. Transmittances of the proposed piezoelectric metamaterial beams with different effective coupling spring stiffnesses: (a) $\epsilon = -0.05$, (b) $\epsilon = -0.15$, (c) $\epsilon = -0.25$, (d) $\epsilon = -0.35$.
In the legend, XCXR is short for X cells and X resonators.

system consists of only limited number of cells. If the damping ratio of the system is reduced and the number of cells of the system is increased, the small dip will disappear. Thus, it can be seen that unlike the band gaps, this small dip is not a reliable vibration-suppression region. In addition, through the same way by reducing the system damping ratio and further increasing the number of cells, the aforementioned third band gap could show up as a vibration-suppression region in the system transmittance. The result of the proposed piezoelectric metamaterial beam consisting of 50 cells is presented in Figure 11(b). Moreover, from Figure 11(b), the broadband property of the proposed piezoelectric metamaterial beam is clearly revealed.

5. A further discussion on system stability

The stability analysis of the standalone 2DOF oscillating sub-system that constitutes the micro-structure of the proposed metamaterial beam has been presented in

section 2.3, and the stability criterion is provided in equation (18). The metamaterial beam system is after all different from and more complicated than the standalone 2DOF oscillating sub-system. In order to remove any concern about the applicability of the derived stability criterion (i.e. equation (18)), a further discussion is supplemented based on a rigorous study of the stability of the entire metamaterial beam system.

The stability of a system can be determined based on the characteristic of its eigenvalues. Eigenvalues having any non-zero imaginary part indicate that the state variables (i.e. displacement and velocity) will evolve without bounds, and the system is thus unstable. The procedure for determining the stability (i.e. the eigenvalues) of the finitely long model is quite straightforward, and various approaches are available to do the calculation. For the infinitely long model, since the band structure analysis is intrinsically an eigenvalue problem (equation (30)), the eigenvalues of the infinitely long model can thereby be obtained from its dispersion

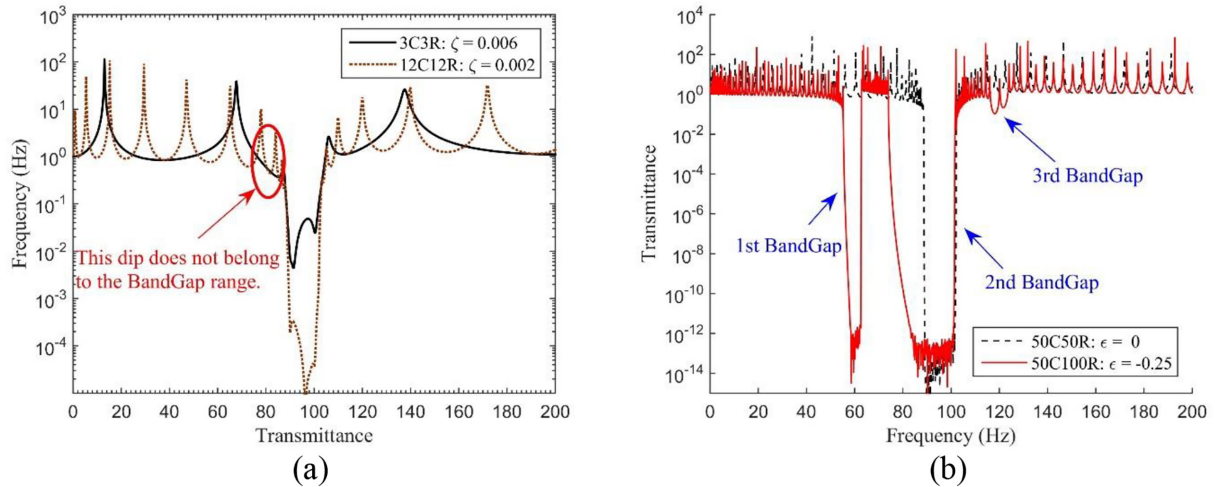


Figure 11. (a) Transmittances of the metamaterial beam without internal couplings for different number of cells and system damping ratios and (b) transmittances of the proposed piezoelectric metamaterial beams consisting of 50 cells. In the legend, XCXR is short for X cells and X resonators.

relation. Since the determination of the band gap is also through the band structure analysis, which is finally transformed into an eigenvalue problem, it is worth briefly reviewing the principle for band gap determination first.

The nature of the wavenumber predicts the spatial characteristics of the wave propagation: a pure real value solution of wavenumber indicates a travelling wave; a pure imaginary value solution of wavenumber infers an evanescent wave whose energy quickly decreases with the propagation distance and is spatially concentrated in the vicinity of the source. Hence, by sweeping ω , simultaneously solving for the wavenumber through equation (30) and checking the nature of the wavenumber, one can determine the band gap range of the metamaterial beam system. If we regard ω as a given parameter, the corresponding wavenumbers can be deemed as spatial eigenvalues to be solved.

The stability characteristic of the undamped metamaterial beam system is reflected by the nature of the temporal eigenvalues (i.e. ω) which predicts the temporal characteristics of the wave propagation: a pure real value solution indicates a time-harmonic wave which testifies the stability of the system; a solution having a non-zero imaginary means that the system is unstable. For the previously used transfer matrix method (TMM) method in section, the common way is to sweep ω and seek for the solution to the wavenumber. Hu et al. (2018a) proposed an FE-based method for obtaining the dispersion relation, in which the calculation procedure is reverse: the band structure is obtained by sweeping the wavenumber and solving for ω . This method is suitable for addressing the stability analysis problem of the infinitely long model. On the contrary, the FE-based method is also convenient for

deriving the eigenvalues of the finitely long model. Therefore, the method presented by Hu et al. (2018a) is adopted for the determination of the system stability for both finitely and infinitely long models. The main procedures are similar to those of the typical FE method. The details of the method regarding the formulation of the eigenvalue problem are referred to a study by Hu et al. (2018a). The findings are summarized based on a series of stability analysis with the aid of the method presented by Hu et al. (2018a).

For the finitely long model, it is found that the critical ϵ for ensuring the system stability is always smaller than -0.5 . It means that the stability criterion for the finitely long model comprising the 2DOF oscillating sub-system is always looser than that of the standalone 2DOF oscillating sub-system presented in section 2 (i.e. equation (18)). This is physically explainable. The stability criterion for the standalone 2DOF oscillating sub-system is derived based on the assumption that the base motion of the two DOFs are independent. While, after the 2DOF oscillating sub-system is implemented onto the host beam to form the finitely long metamaterial beam model, the base motion of the two DOFs cannot be arbitrary and a constraint is yielded from the beam deflection continuity requisite, which improves the stability condition. With the increase of the host beam length by increasing either the number of unit cells or the lattice constant, the critical ϵ increases, that is, the system is more prone to lose the stability. Starting from the aforementioned explanation, this is expected. The longer host beam becomes softer and easier to bend. Therefore, the constraint on the base motion of the two DOFs of the 2DOF oscillating sub-system becomes looser, and the system is thus more likely to lose its stability.

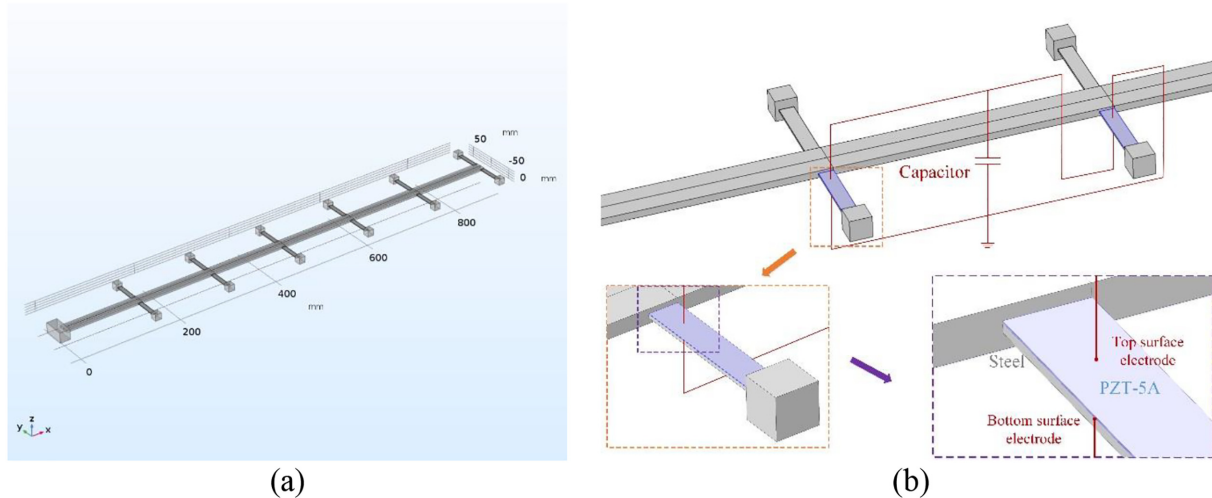


Figure 12. (a) Finite-element model of the proposed piezoelectric metamaterial beam and (b) close-up view of the local resonator.

In terms of the infinitely long model, it has been found that regardless of the parameters of the host beam and the 2DOF oscillating sub-system, as long as ε is tuned smaller than -0.5 , for any given wavenumber, there appears one solution of the temporal eigenvalue (i.e. ω) that contains a non-zero imaginary part. This implies that for the infinitely long model, the stability criterion is the same as that (equation (18)) of the standalone 2DOF oscillating sub-system presented in section 2. In summary, equation (18) (i.e. $\varepsilon > -0.5$) is a sufficient condition for ensuring the stability of both finitely and infinitely long models.

6. Verification by FE method

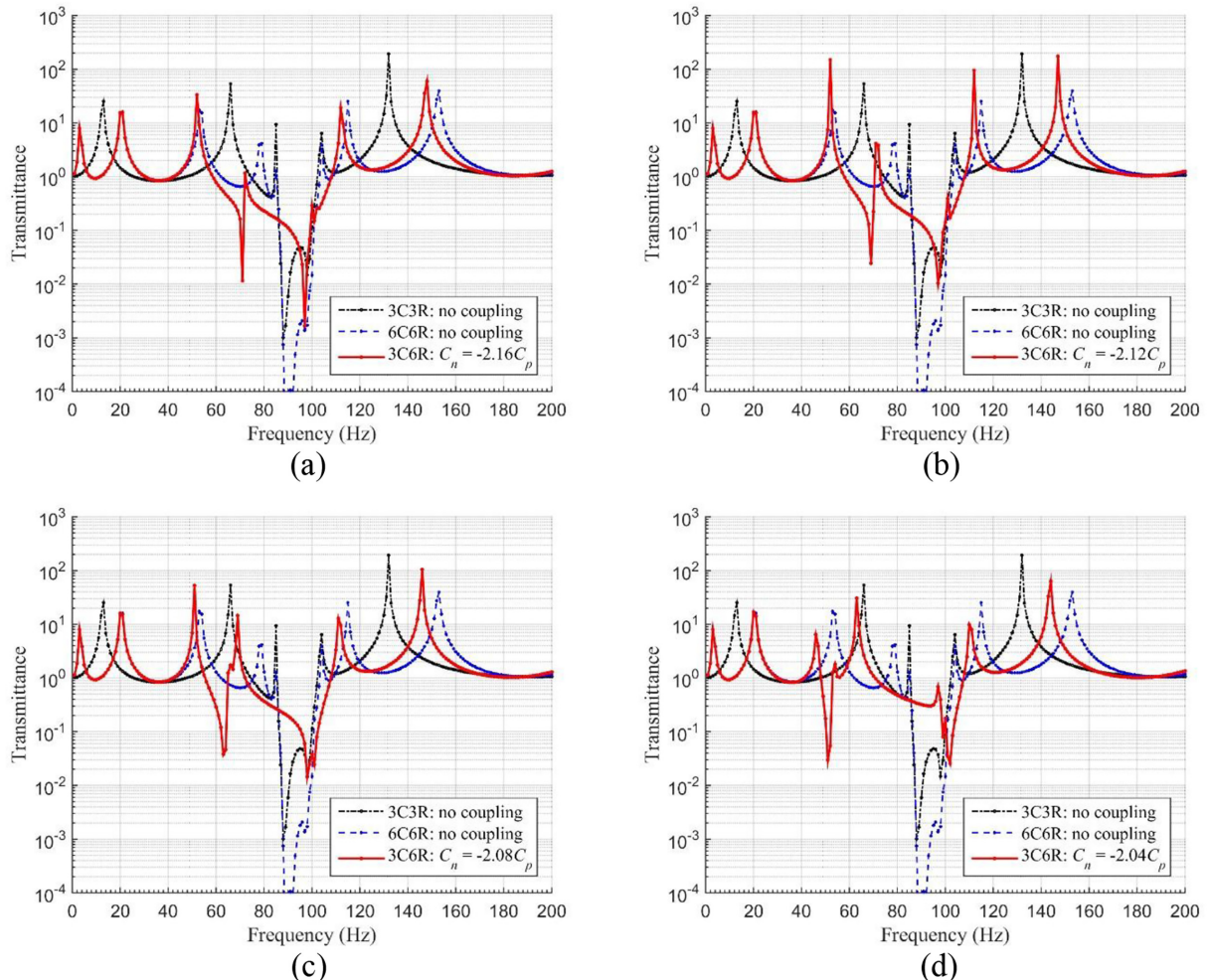
A corresponding FE model of the proposed piezoelectric metamaterial beam is developed as shown in Figure 12(a) using COMSOL to verify the aforementioned analytical predictions. It should be mentioned that the metamaterial beam is designed to have symmetry about the zx plane to prevent the torsional vibration of the host beam, ensured by applying the symmetric boundary condition in the FE model. In the FE model, the local resonators are modelled by cantilevers with tip masses, and the cantilevers are covered by piezoelectric layers. To emulate the electrodes, the top and bottom surfaces of the piezoelectric layer are separately applied with the terminal boundary condition. The circuit connections between the PZTs attached onto two neighbouring resonator beams are implemented using the electrical circuit module of COMSOL. In the electrical circuit module, the external voltages are created by selecting the terminals as the sources. The electrodes are therefore coupled with the electrical circuit which is established by adhering to the circuit diagram as shown in Figure 12(b). The capacitor in the electrical domain

is assigned with a negative value to directly achieve the NC. It is worth mentioning that the theoretical NC shunt circuit is a pure inductive one. In applications, on the contrary, minor resistive load would be included in the shunt yielding small damping. Besides, consider that the op-amps have ultra-small noise in applications, the synthesis of NC would not induce additional noise (uncertainties) in the system either. The geometric and material parameters for the FE model are listed in Table 2.

By applying a displacement excitation to the base, a frequency domain analysis is performed to obtain the transmittance by measuring the responses at the tip of the host beam. Figure 13 shows the FE analysis results for using different NCs -40.12 pF , -39.38 pF , -38.64 pF , and -37.90 pF , (correspondingly $-2.16C_p$, $-2.12C_p$, $-2.08C_p$, and $-2.04C_p$). The FE result of the metamaterial beam without using the shunt capacitance circuit is also provided for comparison. According to the expression of the equivalent coupling stiffness, that is, $K = \theta_1\theta_2/(C_{p1} + C_{p2} + C_n)$, it can be determined that when the NC satisfies $C_n < -2C_p$, the equivalent spring stiffness should be negative. It is worth mentioning that the decrease of $|2C_p + C_n|$ indicates the increase of the $|K|$ (i.e. $|\varepsilon|$). In Figure 13, one can notice the appearance of the additional vibration-suppression region for the cases when there exist NC circuits. As predicted by the analytical analysis, though in theory there exist three band gaps, only two of them produce practical wave-suppression effects, which are demonstrated as suppression regions for the metamaterial beam with limited number of cells. It can be found that with the increase of C_n (i.e. the increase of the coupling stiffness), the additional vibration-suppression region moves towards the lower frequency range. In addition, the width of the additional vibration-suppression region

Table 2. Geometric and material parameters of the finite-element model.

| Geometry parameters | | Material parameters | |
|-------------------------------|----------|---|-----------------------------|
| Host beam length | 0.900 m | Host beam material density | 7850 kg/m ³ |
| Host beam width | 0.020 m | Host beam Young's modulus | 200×10^9 Pa |
| Host beam thickness | 0.004 m | Parasitic beam material density | 7850 kg/m ³ |
| Resonator beam length | 0.0425 m | Parasitic beam Young's modulus | 200 GPa |
| Resonator beam width | 0.008 m | Tip mass material density | 7850 kg/m ³ |
| Resonator beam thickness | 0.001 m | Tip mass Young's modulus | 200×10^9 Pa |
| Tip mass length | 0.0120 m | Piezoelectric material material | PZT-5A |
| Tip mass width | 0.0120 m | Piezoelectric material Young's modulus | 138 GPa |
| Tip mass thickness | 0.0120 m | Strain coefficient of piezoelectric layer | -1.71×10^{-10} C/N |
| Piezoelectric layer length | 0.0425 m | Relative permittivity at constant strain | 1700 |
| Piezoelectric layer width | 0.008 m | | |
| Piezoelectric layer thickness | 0.0002 m | | |

**Figure 13.** Finite-element analysis results of the transmittances for the piezoelectric metamaterial beam with different shunting negative capacitances: (a) $C_n = -2.16C_p$, (b) $C_n = -2.12C_p$, (c) $C_n = -2.08C_p$, and (d) $C_n = -2.04C_p$. In the legend, XCXR is short for X cells and X resonators.

becomes narrower. Besides of that, for the vibration-suppression region around 90 Hz, the width is increased, but the suppression capacity is reduced with

the increase of C_n due to the fact that the valley depth becomes shallower. Comparing Figure 13 with Figure 10, the FE analysis results qualitatively agree with the

analytical predictions very well. Both the appearance of the additional suppression region and the effect of the coupling on the formation of the suppression regions are observed in the FE analysis results as anticipated. It should be mentioned that by considering the stability criterion given by equation (19), the NC C_n cannot be arbitrarily tuned. If $|2C_p + C_n|$ is tuned to be very small, $|\alpha|$ will exceed 0.5 and the system will lose stability. From another point of view, C_n is not suggested to be tuned to make $|2C_p + C_n|$ very small because for the case with too small $|2C_p + C_n|$ (e.g. $C_n = -2.04C_p$ in Figure 13(d)), the additional suppression region becomes too narrow for practical use.

7. Conclusion

This article has proposed a piezoelectric metamaterial beam with shunt capacitance circuit for achieving multiple and tunable band gaps. The underlying mechanism for creating multiple band gaps in the proposed metamaterial beam is by using the shunt capacitance circuit technique to generate internal coupling spring between adjacent local resonators. To ensure the system stability, criterions for tuning the equivalent coupling stiffness and the NC are proposed. Both infinitely long and finite-long models are developed and analytically solved. The effect of the equivalent coupling stiffness on the band gaps and corresponding suppression regions is revealed by both the band structure analysis and the transmittance analysis. It is found that by changing the equivalent coupling stiffness (i.e. the NC), the additional band gap that appears in the low-frequency range can be controlled. By careful selection of an appropriate NC, the proposed metamaterial beam can be tuned to have a broadband vibration-suppression ability. An FE model has also been developed, and the FE results verified the analytical findings.

Declaration of conflicting interests

The author(s) declared no potential conflicts of interest with respect to the research, authorship, and/or publication of this article.

Funding

The author(s) disclosed receipt of the following financial support for the research, authorship, and/or publication of this article: This work is financially supported by the Energy Education Trust of New Zealand (Grant No. 3708242), the PhD scholarship from China Scholarship Council (Grant No. 201608250001), and the start-up funding of Southeast University, Nanjing, China (Grant No. 1122007115).

ORCID iD

Lihua Tang  <https://orcid.org/0000-0001-9031-4190>

References

- Banerjee A, Das R and Calius EP (2017) Frequency graded 1D metamaterials: a study on the attenuation bands. *Journal of Applied Physics* 122(7): 075101.
- Chen S, Wang G and Song Y (2016) Low-frequency vibration isolation in sandwich plates by piezoelectric shunting arrays. *Smart Materials and Structures* 25(12): 125024.
- Chen S, Wang G, Wen J, et al. (2013) Wave propagation and attenuation in plates with periodic arrays of shunted piezo-patches. *Journal of Sound and Vibration* 332(6): 1520–1532.
- Chen S, Wen J, Yu D, et al. (2011) Band gap control of phononic beam with negative capacitance piezoelectric shunt. *Chinese Physics B* 20(1): 014301.
- Chen Y, Hu G and Huang G (2017) A hybrid elastic metamaterial with negative mass density and tunable bending stiffness. *Journal of the Mechanics and Physics of Solids* 105: 179–198.
- Chen Y, Huang G and Sun C (2014) Band gap control in an active elastic metamaterial with negative capacitance piezoelectric shunting. *Journal of Vibration and Acoustics* 136(6): 061008.
- Cheng Z and Shi Z (2014) Vibration attenuation properties of periodic rubber concrete panels. *Construction and Building Materials* 50: 257–265.
- Cheng Z, Shi Z, Mo Y, et al. (2013) Locally resonant periodic structures with low-frequency band gaps. *Journal of Applied Physics* 114(3): 033532.
- De Marneffe B and Preumont A (2008) Vibration damping with negative capacitance shunts: theory and experiment. *Smart Materials and Structures* 17(3): 035015.
- Fang X, Wen J, Bonello B, et al. (2017) Ultra-low and ultra-broad-band nonlinear acoustic metamaterials. *Nature Communications* 8(1): 1288.
- Fang X, Wen J, Yin J, et al. (2016) Wave propagation in nonlinear metamaterial multi-atomic chains based on homotopy method. *AIP Advances* 6(12): 121706.
- Hand T and Cummer S (2007) Characterization of tunable metamaterial elements using MEMS switches. *IEEE Antennas and Wireless Propagation Letters* 6: 401–404.
- Hu G, Tang L and Das R (2018a) General framework for modeling multifunctional metamaterial beam based on a derived one-dimensional piezoelectric composite finite element. *Journal of Aerospace Engineering* 31(6): 04018088.
- Hu G, Tang L and Das R (2018b) Internally coupled metamaterial beam for simultaneous vibration suppression and low frequency energy harvesting. *Journal of Applied Physics* 123(5): 055107.
- Hu G, Tang L, Banerjee A, et al. (2017a) Metastructure with piezoelectric element for simultaneous vibration suppression and energy harvesting. *Journal of Vibration and Acoustics* 139(1): 011012.
- Hu G, Tang L, Das R, et al. (2017b) Acoustic metamaterials with coupled local resonators for broadband vibration suppression. *AIP Advances* 7(2): 025211.
- Huang G and Sun C (2010) Band gaps in a multiresonator acoustic metamaterial. *Journal of Vibration and Acoustics-transactions of the ASME* 132(3): 031003.
- Ji H, Qiu J, Cheng J, et al. (2011) Application of a negative capacitance circuit in synchronized switch damping techniques for vibration suppression. *Journal of Vibration and Acoustics* 133(4): 041015.

- Khajehpourian R and Hussein M (2014) Dispersion characteristics of a nonlinear elastic metamaterial. *AIP Advances* 4(12): 124308.
- Lazarov BS and Jensen JS (2007) Low-frequency band gaps in chains with attached non-linear oscillators. *International Journal of Non-Linear Mechanics* 42(10): 1186–1193.
- Li X, Chen Y, Hu G, et al. (2018) A self-adaptive metamaterial beam with digitally controlled resonators for subwave-length broadband flexural wave attenuation. *Smart Materials and Structures* 27(4): 045015.
- Liu X and Padilla WJ (2013) Dynamic manipulation of infrared radiation with MEMS metamaterials. *Advanced Optical Materials* 1(8): 559–562.
- Liu Y, Yu D, Li L, et al. (2007) Design guidelines for flexural wave attenuation of slender beams with local resonators. *Physics Letters A* 362(5): 344–347.
- OPA445 (2008) Datasheet of OPA445. Available at: <http://www.ti.com/lit/ds/symlink/opa445.pdf>
- Sun H, Du X and Pai PF (2010) Theory of metamaterial beams for broadband vibration absorption. *Journal of Intelligent Material Systems and Structures* 21(11): 1085–1101.
- Tang J and Wang K (2001) Active-passive hybrid piezoelectric networks for vibration control: comparisons and improvement. *Smart Materials and Structures* 10(4): 794–806.
- Thorp O, Ruzzene M and Baz A (2001) Attenuation and localization of wave propagation in rods with periodic shunted piezoelectric patches. *Smart Materials and Structures* 10(5): 979–989.
- Wang G and Chen S (2015) Large low-frequency vibration attenuation induced by arrays of piezoelectric patches shunted with amplifier-resonator feedback circuits. *Smart Materials and Structures* 25(1): 015004.
- Xiao Y, Wen J and Wen X (2012) Longitudinal wave band gaps in metamaterial-based elastic rods containing multi-degree-of-freedom resonators. *New Journal of Physics* 14(3): 033042.
- Xu J and Tang J (2017) Tunable prism based on piezoelectric metamaterial for acoustic beam steering. *Applied Physics Letters* 110(18): 181902.
- Zhang H, Wen J, Xiao Y, et al. (2015) Sound transmission loss of metamaterial thin plates with periodic subwave-length arrays of shunted piezoelectric patches. *Journal of Sound and Vibration* 343: 104–120.
- Zhou W, Wu Y and Zuo L (2015) Vibration and wave propagation attenuation for metamaterials by periodic piezoelectric arrays with high-order resonant circuit shunts. *Smart Materials and Structures* 24(6): 065021.
- Zhu R, Chen Y, Barnhart M, et al. (2016) Experimental study of an adaptive elastic metamaterial controlled by electric circuits. *Applied Physics Letters* 108(1): 011905.
- Zhu R, Liu X, Hu G, et al. (2014) A chiral elastic metamaterial beam for broadband vibration suppression. *Journal of Sound and Vibration* 333(10): 2759–2773.